Supplementary Information

Mechanical decoupling epitaxy via compliant microdisks yields relaxed transferable AlGaN across broad compositions

Pierre-Marie Coulon,[1] Lea Lacomblez,[1] Maud Nemoz,[1] Ileana Florea,[1] Halima Rahmoune,[2] Alexandre Pofelski,[3] Philippe Vennéguès,[1] Sebastien Chenot,[1] Maksym Gromovyi,[1] Nabila Maloufi,[2] Blandine Alloing,[1] Benjamin Damilano[1]*

[1]Université Côte d'Azur, CNRS, CRHEA, Valbonne, France

[2]Université de Lorraine, CNRS, Arts et Métiers, LEM3, Metz, France

[3] Canadian Centre for Electron Microscopy, McMaster University, Hamilton, Ontario L8S 4M1, Canada

Supplementary Figures and calculation

Shape of the microdisk after thermal etching

Fig.S1b presents a high-magnification cross-sectional SEM image of the $Al_{0.15}Ga_{0.85}N$ microdisks following thermal etching, clearly evidencing edge-induced bending and deformation of the microdisk. Minor residual by-products from the GaN thermal etching are observed on the −c $Al_{0.15}Ga_{0.85}N$ surface. Note that the shape of the resulting GaN pillars appears to follow that of the initial $Al_{0.15}Ga_{0.85}N$/GaN micropillars with a fairly straight profile in the upper half part, and a slightly slanted profile in the bottom half part (FigS1a.). Although a hexagonal structure can be observed from the top of the $Al_{0.15}Ga_{0.85}N$ microdisk in Fig1.b and I (due to the change of contrast induced by the transparency to electrons of the thin $Al_{0.15}Ga_{0.85}N$ membrane), the GaN pillar does not present well-defined non-polar or semi-polar facet after thermal etching.

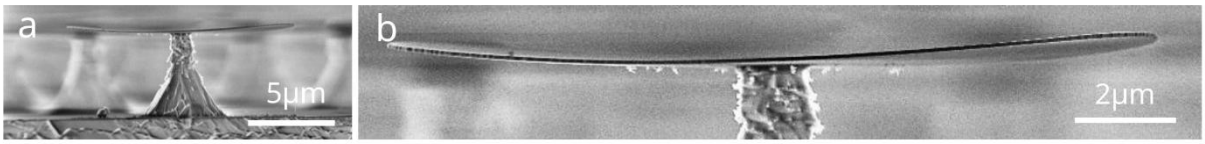

Fig.S1. High magnification cross-section SEM images of an $Al_{0.15}Ga_{0.85}N$ microdisk revealing its deformation and bending after thermal etching.

Composition of *+c* and *-c* $Al_{0.5}Ga_{0.5}N$ regrowth

Fig.S2 shows four EDX composition maps acquired at different locations across the $Al_{0.15}Ga_{0.85}N$ microdisk interface with the Al-polar (+*c*) and N-polar (−*c*) $Al_xGa_{1-x}N$ regrowth.. The $Al_{0.15}Ga_{0.85}N$ microdisk maintains a homogeneous composition from centre to edge, while

the Al content of both regrowth polarities varies slightly between 50% and 52%. Notably, a pronounced compositional gradient is detected over the first 100–150 nm of the +*c* $Al_xGa_{1-x}N$ regrowth, likely arising from strain-driven compositional adjustment during the early stages of epitaxial overgrowth.

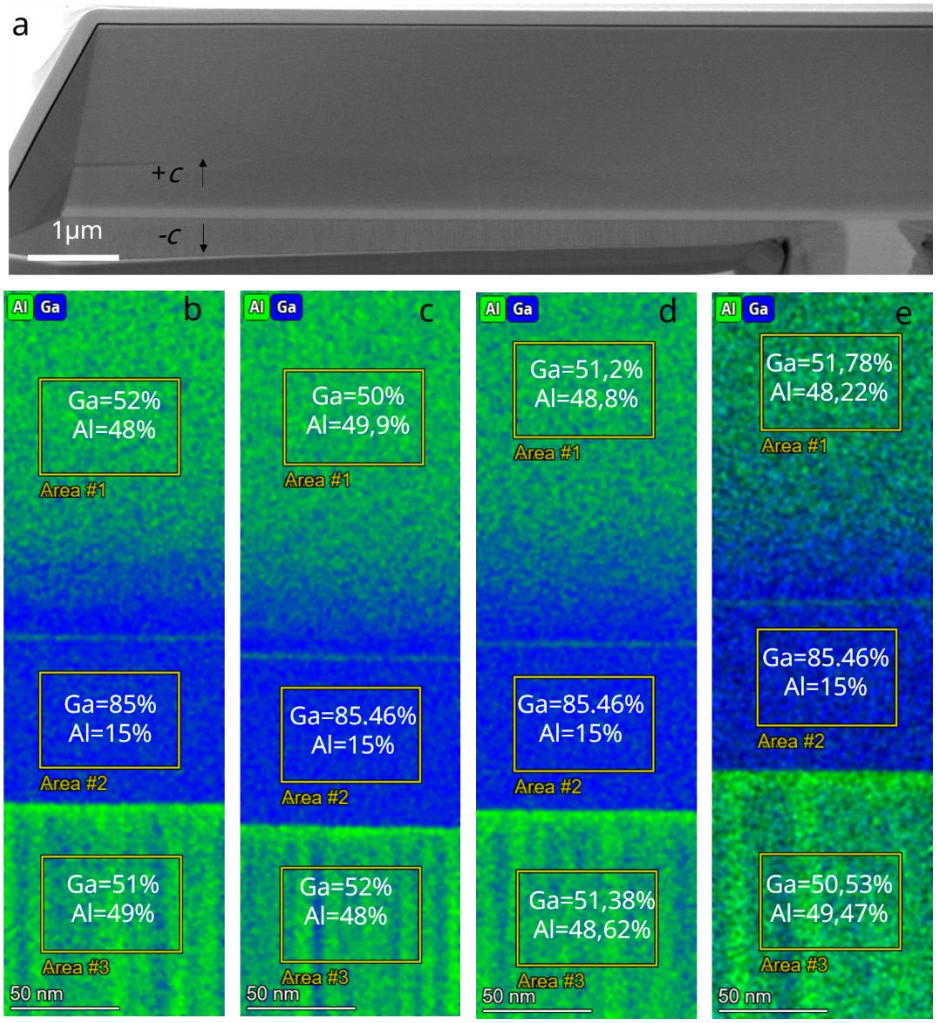

Fig.S2. EDX chemical maps acquired at various locations of the interface between the $Al_{0.15}Ga_{0.85}N$ microdisk and the Al-polar and N-polar of the 2,5 µm thick $Al_{0.5}Ga_{0.5}N$ micropallet.

Surface morphology and dislocation density across the process flow

Fig.S3 summarizes the surface morphology evolution across the fabrication process as revealed by AFM. Figures S3a–d show 4 µm × 4 µm topography images, with corresponding phase maps displayed in Figures S3e–h, acquired on the $Al_{0.15}Ga_{0.85}N$/GaN micropillar, the $Al_{0.15}Ga_{0.85}N$ microdisk, and the 1 µm- and 5 µm-thick $Al_{0.5}Ga_{0.5}N$ micropallets (Fig.2a–d). Threading dislocations manifest as dark features in the topographic images and as bright, island-like contrast in the phase maps. Larger-area AFM scans (25 µm × 25 µm; Figures S3i–l) highlight a surface morphology changing to hillock-type growth for $Al_{0.5}Ga_{0.5}N$ regrowth.

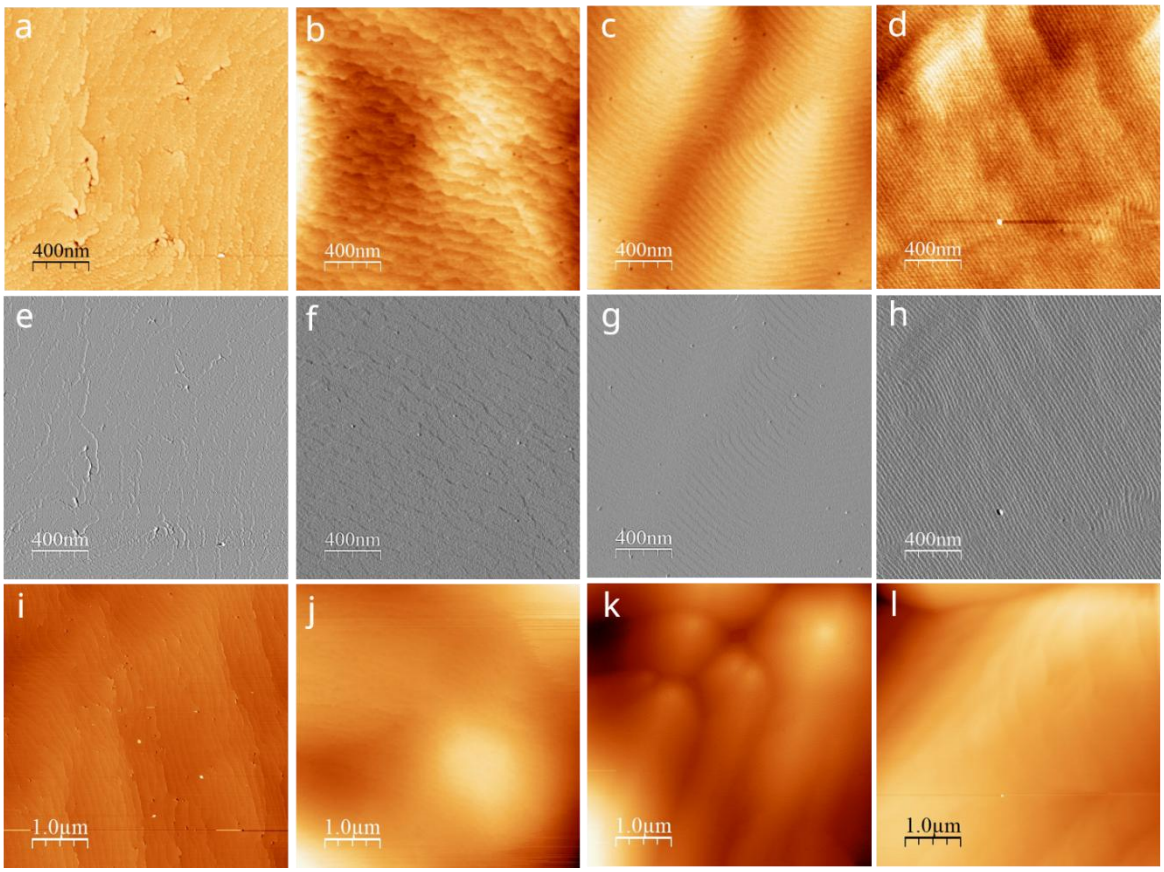

Fig.S3. 4 µm^2 AFM scan carried out on the *c*-plane surface of a) $Al_{0.15}Ga_{0.85}N$/GaN micropillar, b) $Al_{0.15}Ga_{0.85}N$ microdisk, c) 1 µm and d) 5 µm thick $Al_{0.5}Ga_{0.5}N$ micropallet. 4 µm^2 phase scan carried out on the *c*-plane surface of e) $Al_{0.15}Ga_{0.85}N$/GaN micropillar, f) $Al_{0.15}Ga_{0.85}N$ microdisk, g) 1 µm and h) 5 µm thick $Al_{0.5}Ga_{0.5}N$ micropallet. 25 µm^2 AFM scan carried out on the *c*-plane surface of i) $Al_{0.15}Ga_{0.85}N$/GaN micropillar, j) $Al_{0.15}Ga_{0.85}N$ microdisk, k) 1 µm and l) 5 µm thick $Al_{0.5}Ga_{0.5}N$ micropallet.

Surface morphology and dislocation density of GaN on sapphire template

Fig.S4.a and b presents a 2 µm × 2 µm and 5 µm × 5 µm AFM topography image of a 5 µm-thick GaN layer grown on sapphire. The 4 µm^2 scan reveals mixed- or screw-type threading dislocations (eight identified) together with edge-type dislocations (five identified, marked by white arrows). From this area, a threading dislocation density of 3.25 x 10^8 cm^{-2} is extracted, consistent with the dislocation densities measured in the subsequent overgrown $Al_xGa_{1-x}N$ layers. Fig.S4.c present one of the several ECC micrograph acquired on 5 µm-thick GaN layer grown on sapphire for which a TDD of 2.3 x 10^8 cm^{-2} has been extracted. The average TDD on the several ECC micrograph correspond to the value of 2.2 x 10^8 cm^{-2} indicated in Table 1.

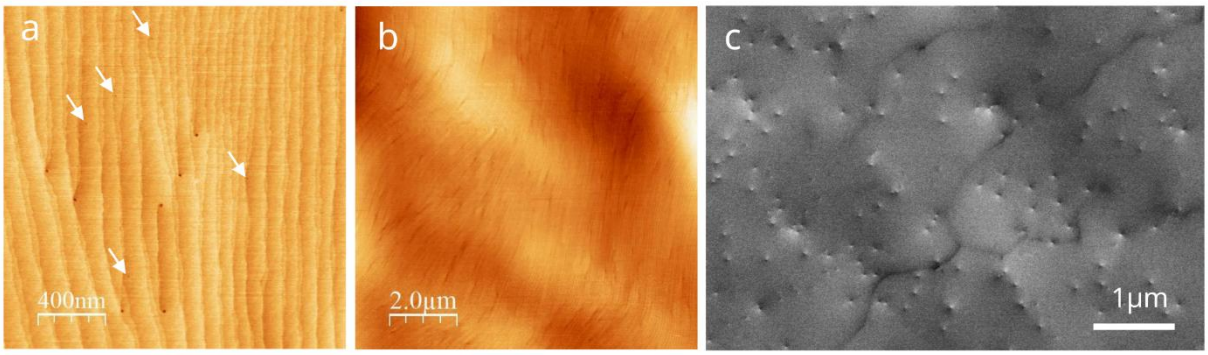

Fig.S4. a) 4 µm^2 and b) 25 µm^2 AFM scan carried out on the *c*-plane surface of a 5 µm GaN on sapphire template. White arrows in a) highlight edge type dislocations while other pits observed on the AFM scan are related to screw or mixed TDs. c) 12.8° tilted ECC micrograph of a 5 µm GaN on sapphire template.

Identification of a-type dislocation in GaN pillar supporting $Al_{0.15}Ga_{0.85}N$ microdisks

Fig.S5 shows dark-field and HRSTEM images acquired near the $Al_{0.15}Ga_{0.85}N$/GaN interface for the $Al_{0.82}Ga_{0.18}N$ regrowth on the TEM lamella presented in Fig.1m and 2k. The dislocations are visible in contrast under the g = $\bar{1}100$ diffraction condition (Fig. S5a) and extinguish under the g = 0002 condition (Fig. S5c), indicating, according to the dislocation extinction criterion, that they correspond to a-type dislocations. The Burgers circuit shown in Fig. S5d further confirms this assignment through the observed closure failure consistent with an a-type Burgers vector.

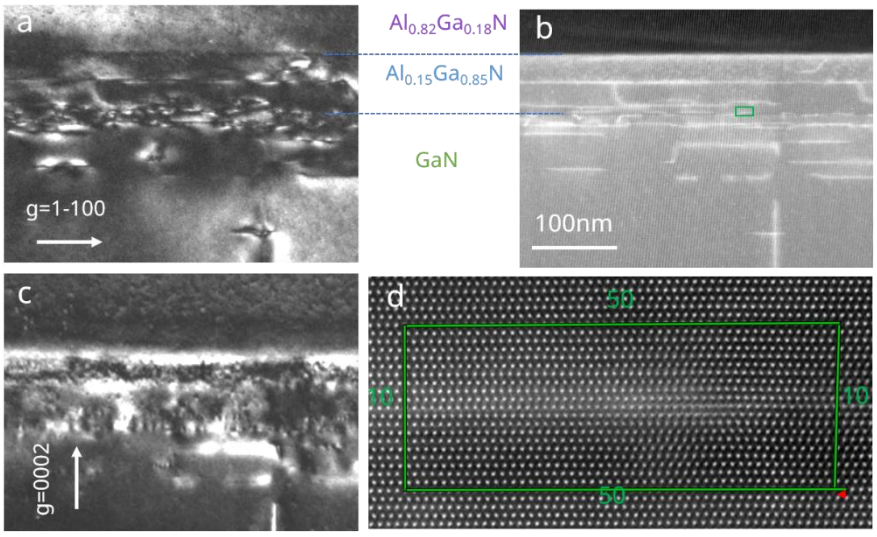

Fig.S5. Dark field imaging along the a) 1-100 zone axis and c) 0002 zone axis of the STEM image in b). d) HRSTEM image of an a-type dislocation.4 µm^2 and b) 25 µm^2 AFM scan carried out on the *c*-plane surface of a 5 µm GaN on sapphire template. White arrows in a) highlight edge type dislocations while other pits observed on the AFM scan are related to screw or mixed TDs. c) 12.8° tilted ECC micrograph of a 5 µm GaN on sapphire template.

STEM Moiré for strain determination over a wide field of view

Fig.S6 presents an overview STEM Moiré image of the 2.5 µm-thick $Al_{0.82}Ga_{0.18}N$ micropallet, with the locations of the four STEM Moiré acquisitions used for Fourier-based strain analysis superimposed. Low-magnification acquisitions (blue and red) probe the spatial strain distribution within the $Al_{0.82}Ga_{0.18}N$ regrowth and the $Al_{0.15}Ga_{0.85}N$ microdisk , whereas high-magnification acquisitions (purple and green) focus on the local strain state of the underlying $Al_{0.15}Ga_{0.85}N$ microdisk.

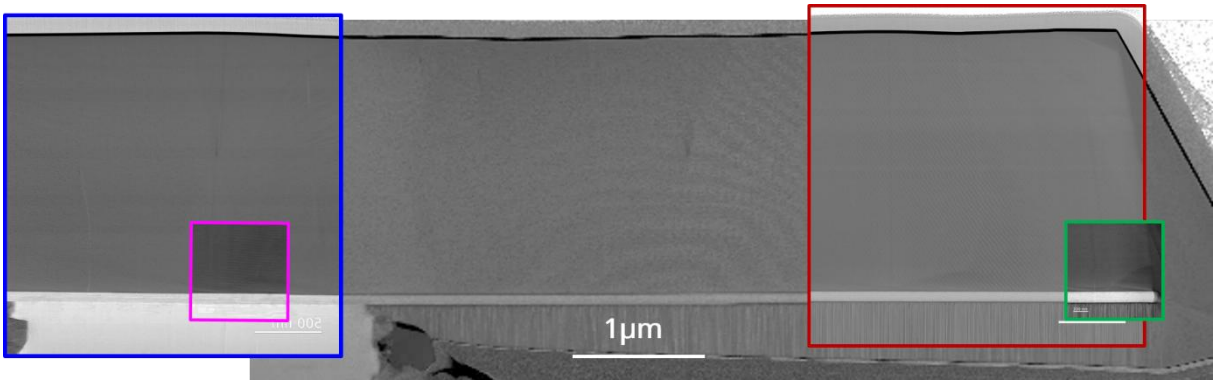

Fig.S6. Large field of STEM Moiré image overlapped with images described in Fig.4 and S7: in blue Fig.4a, in red Fig.4e, in purple Fig.S7k and in green Fig.S7p.

After Fourier filtering of the Moiré fringes to isolate the selected crystallographic orientation, the local phase was extracted, and spatial derivatives yielded the in-plane ε_a (Fig.S7d, i, n, and s) and out-of-plane ε_c (Fig.S7e, j, o and t) strain components with several nanometers resolution. The theoretical in and out-of plane lattice parameter of the $Al_{0.82}Ga_{0.18}N$ regrowth (a = 3,1254 A, c = 5,0163 A) is taken as a reference as this later is found to be relaxed from XRD experiments. The central part of the $Al_{0.82}Ga_{0.18}N$ regrowth is taken as the reference. Fig.S7b, g, l, and q show the resulting in plane lattice parameter *a* while Fig.S7c, h, m and r present the out of plane lattice parameter *c*.

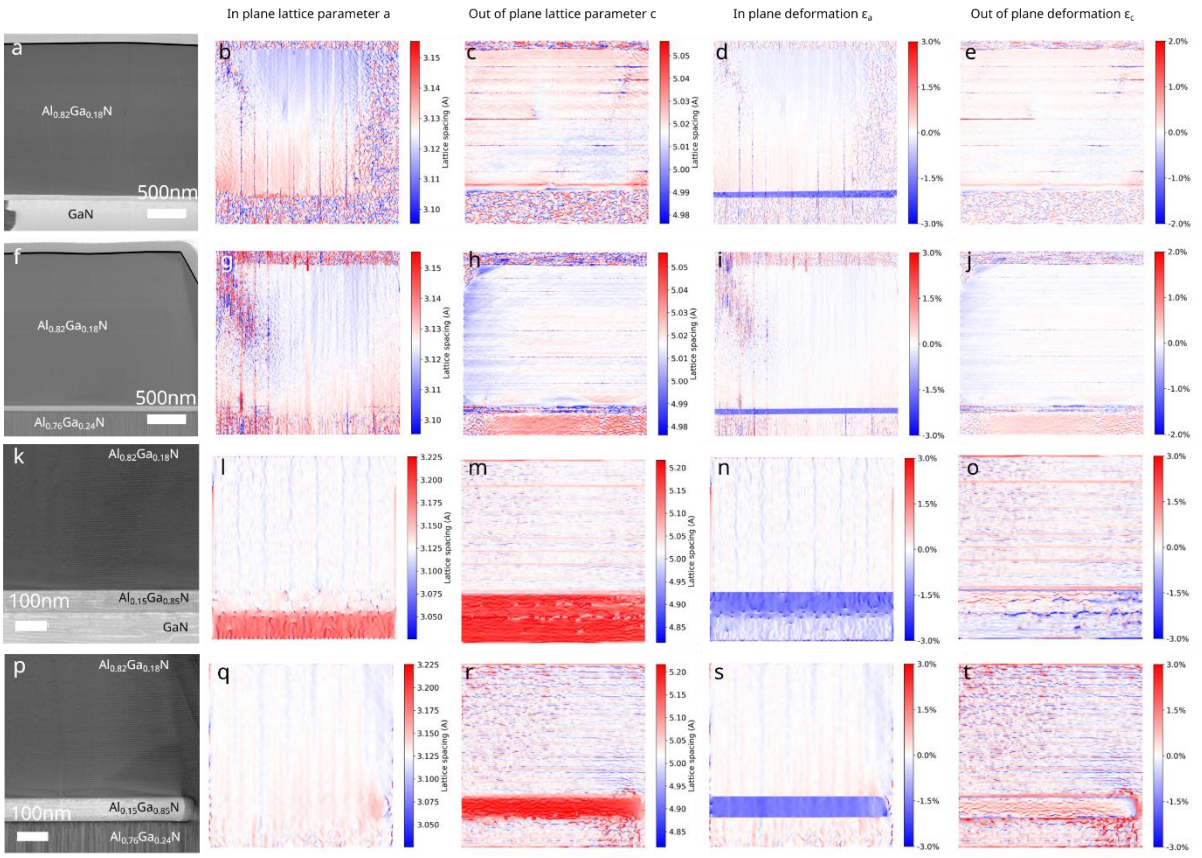

Fig.S7. (a,d) Low-magnification STEM Moiré images acquired above the GaN pillar (a) and at the micropallet extremity (d). (b,g) Corresponding in-plane lattice parameter *a*. (e,j) Corresponding out of-plane lattice parameter *c*. (d,i) Corresponding in-plane strain (ε_a) maps. (e,j) Corresponding out of-plane strain (ε_c) maps. (k,p) High-magnification STEM Moiré images acquired at the same locations. (l,q) Corresponding in-plane lattice parameter *a*. (m,r) Corresponding out of-plane lattice parameter *c*. (n,s) Corresponding in-plane strain (ε_a) maps. (o,t) Corresponding out of-plane strain (ε_c) maps.

Strain-Induced Near-Band-Edge Energy Shift in $Al_{0.15}Ga_{0.85}N$

1.1. Strain state and elastic relations

We consider a wurtzite $Al_{0.15}Ga_{0.85}N$ layer grown along the c-axis (0001) and subjected to biaxial in-plane strain, as typically encountered in epitaxial films or compliant microstructures. The strain tensor components are written as:

$$\varepsilon_{xx} = \varepsilon_{yy} = \varepsilon_{\parallel}, \qquad \varepsilon_{zz} \neq 0 \qquad \text{(eq.1)}$$

Assuming a free surface along the growth direction, the out-of-plane stress vanishes ($\sigma_{zz} = 0$). Using Hooke's law for hexagonal crystals, this leads to the standard relation:

$$\sigma_{zz} = C_{13}(\varepsilon_{xx} + \varepsilon_{yy}) + C_{33}\varepsilon_{zz} = 0$$

which gives:

$$\varepsilon_{zz} = -2\,\frac{C_{13}}{C_{33}}\,\varepsilon_{\parallel} \qquad \text{(eq.2)}$$

Elastic constants for $Al_{0.15}Ga_{0.85}N$ are obtained by linear interpolation between GaN and AlN values reported in the literature.

$$C_{ij}(x) = (1-x)C_{ij}^{GaN} + xC_{ij}^{AlN}$$

Using $C_{13}^{GaN} = 103\ GPa$, $C_{33}^{GaN} = 398\ GPa$, $C_{13}^{AlN} = 108\ GPa$, $C_{33}^{AlN} = 373\ GPa$, for x=0.15, we obtain:

$$\frac{C_{13}}{C_{33}} \approx 0.264$$

$$\varepsilon_{zz} \approx -0.53\ \varepsilon_{\parallel} \quad \text{(eq.3)}$$

1.2. Deformation-potential formalism

Following Yan et al. [1], the strain-induced shifts of the conduction and valence bands are described using the Bir–Pikus Hamiltonian for wurtzite semiconductors. The NBE transition is assumed to involve the conduction-band minimum and the uppermost valence band (A band), which dominates optical emission in compressively strained *c*-plane GaN and low-Al-content AlGaN.

The NBE energy is:

$$E_{NBE} = E_c - E_{v,A}$$

So that the strain-induced shift is:

$$\Delta E_{NBE} = \Delta E_c - \Delta E_{v,A} \quad \text{(eq.4)}$$

1.2. Conduction band shift

Purely hydrostatic:

$$\Delta E_c = a_{ct}(\varepsilon_{xx} + \varepsilon_{yy}) + a_{cz}\varepsilon_{zz} \quad \text{(eq.5)}$$

where:

a_{ct} and a_{cz} are the conduction band deformation potentials

1.3. Valence-band A shift

The valence bands shift due to hydrostatic strain, uniaxial strain and crystal-field + spin-orbit. The diagonal terms contain:

$$D_1\varepsilon_{zz} + D_2(\varepsilon_{xx} + \varepsilon_{yy})$$

Plus, band mixing (D3-D6)

For typical epitaxial strain (<1%), the A valence band remains mostly pure |X+iY⟩ character so its shift is dominated by the diagonal term:

$$\Delta E_{v,A} = D_1\varepsilon_{zz} + D_2(\varepsilon_{xx} + \varepsilon_{yy}) \quad \text{(eq.6)}$$

1.4. Evaluation of the NBE shift

Inserting eq.5 and 6 into eq.4 yields the following NBE shift:

$$\Delta E_{NBE} = (a_{ct} - D_2)(\varepsilon_{xx} + \varepsilon_{yy}) + (a_{cz} - D_1)\,\varepsilon_{zz} \quad \text{(eq.7)}$$

Substituting eq.1, 2 and 3 in to eq.7 yields the following NBE shift for $Al_{0.15}Ga_{0.85}N$:

$$\Delta E_{NBE} = 2((a_{ct} - D_2) - 0.53(a_{cz} - D_1))\,\varepsilon_{\parallel} \quad \text{(eq.8)}$$

Taking the HSE recommended deformation potential parameters of Yan et al and performing linear extrapolation:

$$(a_{cz} - D_1)(x) = (1-x)(a_{cz} - D_1)^{GaN} + x(a_{cz} - D_1)^{AlN}$$

$$(a_{ct} - D_0)(x) = (1-x)(a_{ct} - D_2)^{GaN} + x(a_{ct} - D_2)^{AlN}$$

Using $(a_{cz} - D_1)^{GaN} = -6.7$, $(a_{ct} - D_2)^{GaN} = -8.88$, $(a_{cz} - D_1)^{AlN} = -4.36$,$(a_{ct} - D_2)^{AlN} = -12.35$, we obtain:

$$(a_{cz} - D_1)^{Al0.15Ga0.85N} = 0.85(-6.7) + 0.15(-4.36) = -6.39$$

$$(a_{ct} - D_2)^{Al0.15Ga0.85N} = 0.85(-8.88) + 0.15(-12.35) = -9.4$$

Therefore, using eq.8, the total NBE shift for $Al_{0.15}Ga_{0.85}N$ is:

$$\Delta E_{NBE} = 2((-9.4) - 0.53(-6.39))\,\varepsilon_{\parallel}$$

$$\Delta E_{NBE} \approx -12\varepsilon_{\parallel}\ \text{(eV)} \quad \text{(eq.9)}$$

1.7. Extracted in-plain strain from optical bandgap shifts obtain by CL experimental data

From CL experiment, we consider an emission of 327.5 nm as the relaxed NBE of the $Al_{0.15}Ga_{0.85}N$ microdisk. We then have emission ranging between 320 and 318 nm when $Al_{0.5}Ga_{0.5}N$ is regrown upon $Al_{0.15}Ga_{0.85}N$ microdisk and emission ranging between 317.5 and 316 nm for $Al_{0.82}Ga_{0.18}N$ regrowth.

Using:

$$\text{E(eV)} = \frac{1240}{\lambda(nm)} \quad \text{(eq.10)}$$

The NBE shift of the $Al_{0.15}Ga_{0.85}N$ upon $Al_{0.5}Ga_{0.5}N$ regrowth is:

$$\Delta E_{NBE} = 3.899 - 3.786 = +0.113\ eV \quad \text{(eq.11)}$$

$$\Delta E_{NBE} = 3.875 - 3.786 = +0.089\ eV \quad \text{(eq.12)}$$

Substituting equation (eq.11 and 12) into equation (eq.9) result in an in-plain strain of:

$$\varepsilon_{\parallel} = \frac{0.113}{12} \approx -0.95\% \quad \text{(eq.13)}$$

$$\varepsilon_{\parallel} = \frac{0.089}{12} \approx -0.75\% \quad \text{(eq.14)}$$

The NBE shift of the $Al_{0.15}Ga_{0.85}N$ upon $Al_{0.82}Ga_{0.18}N$ regrowth is:

$$\Delta E_{NBE} = 3.924 - 3.786 = +0.138\ eV \quad \text{(eq.15)}$$

$$\Delta E_{NBE} = 3.905 - 3.786 = +0.119\ eV \quad \text{(eq.16)}$$

Substituting equation (eq.15 and 16) into equation (eq.9) result in an in-plain strain of:

$$\varepsilon_{\parallel} = \frac{0.138}{12} \approx -1.15\% \quad \text{(eq.17)}$$

$$\varepsilon_{\parallel} = \frac{0.119}{12} \approx -1\% \quad \text{(eq.18)}$$

Optical properties across the process flow and single $Al_{0.5}Ga_{0.5}N$ micropallets

The optical properties of the microstructure created across the process were assessed by room temperature CL, as displayed in Fig.S8. Figure S8.e presents the spectra acquired at half-radius of each microstructure, as pointed out by the empty circle in the panchromatic CL images in Fig.S8a, b, c and d. All spectra exhibit well defined near band edge (NBE) emission as well as two defect band related emission. $Al_{0.15}Ga_{0.85}N$/GaN micropillar black spectra reveals the GaN and $Al_{0.15}Ga_{0.85}N$ NBE at 360,5 nm and 330,5 nm, respectively, as well as two defect band, one at ≈ 560 nm being the common yellow band (YB) observed in GaN template [2], and another one at ≈ 445 nm originating from cation vacancy complex with one-negative charge (V_{III} complex)$^{1-}$, such as $(V_{Ga}–2O_N)^{1-}$ or related complexes in the $Al_{0.15}Ga_{0.85}N$ [3, 4]. Panchromatic CL image in Fig.5a highlights the presence of dark spot, which are non-radiative recombination centres ascribed to threading dislocations [5, 6, 7], with a density in the low 10^8 cm^{-2}, in agreement with previous estimations by AFM and ECC micrographs.

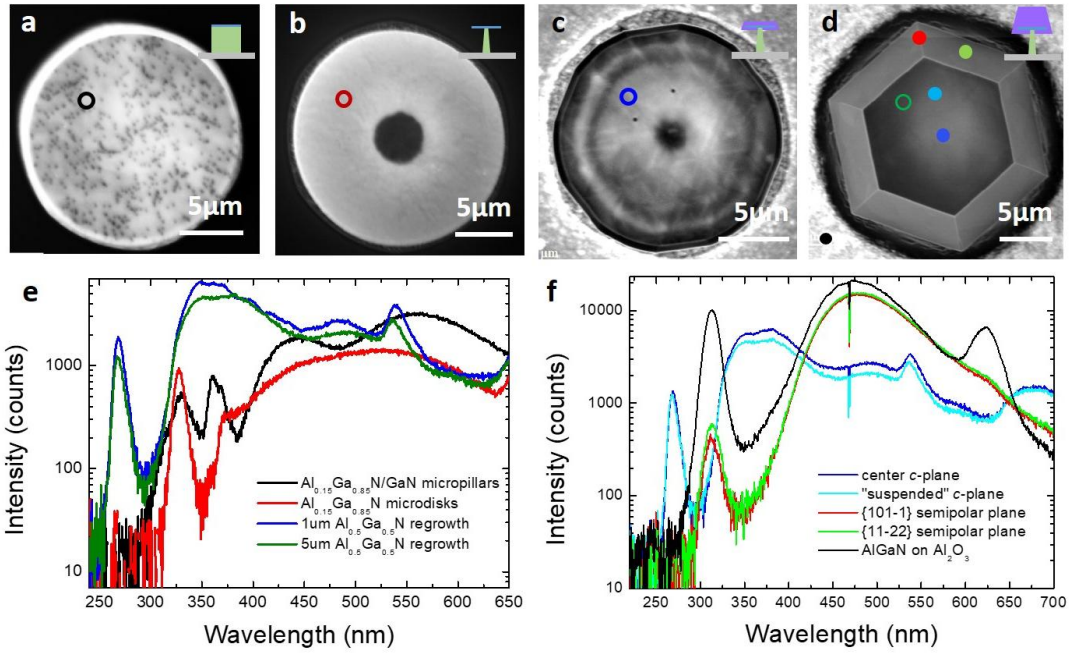

Fig.S8. Panchromatic CL image of a) $Al_{0.15}Ga_{0.85}N$/GaN micropillar, b) $Al_{0.15}Ga_{0.85}N$ microdisk, c) 1µm and d) 5µm thick $Al_{0.5}Ga_{0.5}N$ micropallet. The microstructure is recalled in the upper right part for clarity. e) Single CL spectra acquired on the $Al_{0.15}Ga_{0.85}N$/GaN micropillar, $Al_{0.15}Ga_{0.85}N$ microdisk, 1µm and 5µm thick $Al_{0.5}Ga_{0.5}N$ micropallet. The empty coloured circle in a), b), c) and d) is associated to the spectra in e). f) Single CL spectra acquired at various position across the surface of the 4µm thick $Al_{0.5}Ga_{0.5}N$ regrowth highlighted by a full coloured circle in d).

After thermal etching and GaN removal, the $Al_{0.15}Ga_{0.85}N$ NBE is found to blue shift, in

agreement with strain relaxation of the $Al_{0.15}Ga_{0.85}N$ layer previously observed by XRD in Fig.3b. Single-point spectra reveal a ~2 nm difference in NBE wavelength between the pillar-supported centre and the suspended regions (Fig.S9), a contrast that persists after regrowth, indicating a greater degree of strain relaxation in the suspended part compared with the $Al_{0.15}Ga_{0.85}N$ section located above the GaN pillar. Note that hyperspectral mapping on such thin $Al_{0.15}Ga_{0.85}N$ microdisk standing on sapphire is not possible due to strong charging effect. Alternative transfer on host substrate leads to fracture of the thin $Al_{0.15}Ga_{0.85}N$ microdisk which is far much less robust than the regrown micropallets. The shape of the defect bands also evolves after thermal etching with first, the same contribution already observed around ≈ 445 nm for the $Al_{0.15}Ga_{0.85}N$/GaN micropillar, and second, an additional emission around 530 nm, probably hindered by the GaN YB in the $Al_{0.15}Ga_{0.85}N$/GaN micropillar spectra, and which is ascribed to the same YB in $Al_{0.15}Ga_{0.85}N$, which is known to blue shift with increasing Al content, as for all point defects [3, 4, 8]. The panchromatic CL image of $Al_{0.15}Ga_{0.85}N$ microdisks (Fig.S8b) doesn't display dark spot anymore, but instead dark lines that seems to propagate from the centre to the edge of the microdisks, or vice versa. These lines are likely introduced during thermal etching as the GaN pillar diameter shrinks. After $Al_{0.5}Ga_{0.5}N$ regrowth, both thickness present similar emission spectra with first, an $Al_{0.5}Ga_{0.5}N$ NBE at 268-269 nm, and second, two defect bands around 350-370 nm and at ≈ 485 nm. These two defect bands are more likely to be the one previously observed for the $Al_{0.15}Ga_{0.85}N$ microdisks, the $(V_{III}$ complex$)^{1-}$ and the YB, but blue shifted due to increased Al composition [3, 4, 8]. CL panchromatic image of 1µm thick $Al_{0.5}Ga_{0.5}N$ micropallet reveals the footprint of the GaN pillar at the centre and the presence of bright line on the *c*-plane surface, which could arise from surface morphology and hillocks growth. Note that TDs cannot be seen either for 1µm and 5µm thick $Al_{0.5}Ga_{0.5}N$ micropallet (Fig.S8c and d), probably due to multiple variation in intensity of CL panchromatic image, especially the one coming from $Al_{0.5}Ga_{0.5}N$ regrowth occurring on the sapphire. Single spectra have also been acquired at various position for the 5µm thick $Al_{0.5}Ga_{0.5}N$ micropallet and are presented in Fig.S8f. On one side, the two spectra recorded on the *c*-plane surface present similar emission features as the one already observed for the 1µm thick micropallet, suggesting fairly good and homogeneous optical properties of the $Al_{0.5}Ga_{0.5}N$ regrowth. On the other side, the spectra acquired on the {101-1} semipolar plane, at the junction between two {101-1} semipolar plane (i.e the {11-22} semi-polar plane) and on the $Al_{0.5}Ga_{0.5}N$ regrowth which took place on the etched thermally treated sapphire surface display similar spectra with one emission band centred around 311-314 nm and another one at ≈ 473 nm with an intensity more than one order of magnitude higher than the one of the $Al_{0.5}Ga_{0.5}N$ NBE on the *c*-plane.

As the Al composition on the semipolar plane is higher than 50%, as revealed by the darker contrast of semipolar growth observed in the STEM-HAADF image (Fig.S2a), the emission centred around 311-314 nm cannot be ascribed to the semipolar $Al_xGa_{1-x}N$ NBE emission but rather to the $(V_{III}$ complex$)^{1-}$, which are also blue shifting for semi polar orientation [9]. As a result, the optical properties of the $Al_xGa_{1-x}N$ regrowth taking place on the +*c*-plane appears to have greater optical properties than the one on semi-polar planes and sapphire.

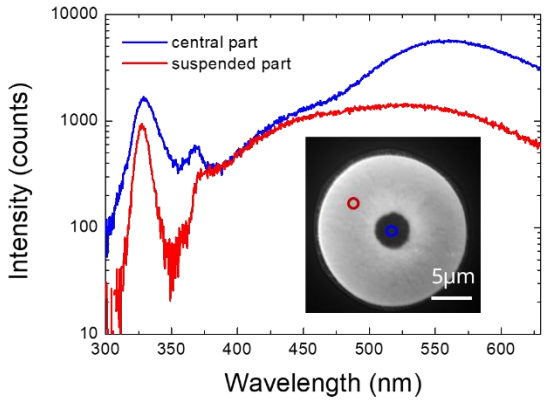

Fig.S9. Single CL spectra acquired at two positions on the $Al_{0.15}Ga_{0.85}N$ microdisk, in red on the suspended part and in blue above the GaN pillar. Inset show the panchromatic CL image the $Al_{0.15}Ga_{0.85}N$ microdisk.

Hyperspectral mapping of $Al_{0.15}Ga_{0.85}N$ microdisk upon $Al_{0.5}Ga_{0.5}N$ and $Al_{0.82}Ga_{0.18}N$ regrowth

Fig.S9 presents the hyperspectral cartography performed on the 1µm thick $Al_{0.5}Ga_{0.5}N$ (Fig.S9a) and 2,5 µm thick $Al_{0.82}Ga_{0.18}N$ (Fig.S9a) micropallets transfered unto carbon tape. Transfer onto carbon enables stable, drift-free hyperspectral mapping, in contrast to measurements on standing microstructures on sapphire. In this configuration the panchromatic image is dominated by the microdisk emission, revealing dark spots associated with threading dislocations, as well as dark line features likely introduced during thermal etching as the GaN pillar diameter shrinks. These features are observed in the intensity map in Fig.S9b. The absence of such dark spots and lines features for the higher composition regrowth could be due to the higher thickness of the -*c* regrowth. Other than that the the two regrowth similar features for the FWHM and the wavelength position of the microdisk's NBE. Only the wavelength range changes due to increased strained imposed by the regrowth, as clearly highlighted in the two map having the same scale bar.

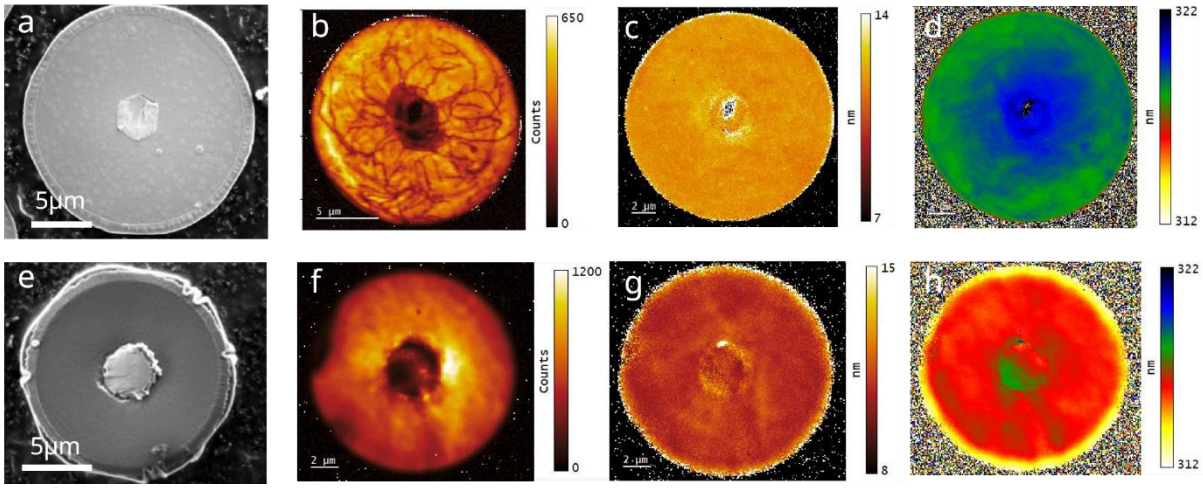

Fig.S10. Plan view SEM images of a a) 1 µm thick $Al_{0.5}Ga_{0.5}N$ micropallet and e) 2.5 µm thick $Al_{0.82}Ga_{0.18}N$ micropallet transferred on carbon tape. Hyperspectral cartography of the $Al_{0.15}Ga_{0.85}N$ NBE b and f) intensity, c and g) FWHM and d and h) emission wavelength position for $Al_{0.5}Ga_{0.5}N$ and $Al_{0.82}Ga_{0.18}N$ regrowth, respectively.

[1] Yan, Q. et al. Effects of strain on the band structure of group-III nitrides. *Phys. Rev. B* **90**, 125118 (2014).
[2] M. A. Reshchikov, H. Morkoç. Luminescence properties of defects in GaN. *J. Appl. Phys.* **97**(6), 061301 (2005)
[3] Nepal, N. et al. Photoluminescence studies of impurity transitions in AlGaN alloys. *Appl. Phys. Lett.* **89** (9) 092107 (2006).
[4] Jiang, K. et al. Suppressing the luminescence of Vcation-related point-defect in AlGaN grown by MOCVD on HVPE. *Applied Surface Science* **520**,146369 (2020).
[5] Rosner, S. J. et al. Correlation of cathodoluminescence inhomogeneity with microstructural defects in epitaxial GaN grown by metalorganic chemical-vapor deposition. *Appl. Phys. Lett.* **70** (4) 420–422 (1997).
[6] Naresh-Kumar, G. et al. Coincident Electron Channeling and Cathodoluminescence Studies of Threading Dislocations in GaN, *Microscopy and Microanalysis*, **20**(1), 55–60 (2014).
[7] Lähnemann, J. et al. Carrier diffusion in GaN a cathodoluminescence study. III: Nature of nonradiative recombination at threading dislocations. *Phys. Rev. Applied* **17**(2), 024019 (2020).
[8] Nam, K. B. et al. Deep impurity transitions involving cation vacancies and complexes in AlGaN alloys. *Appl. Phys. Lett.* **86** (22) 222108 (2005).
[9] Spasevski, L. et al. A systematic comparison of polar and semipolar Si-doped AlGaN alloys with high AlN content. *J. Phys. D: Appl. Phys.* **54,** 035302 (2021).